RSC Advances

PAPER

View Article Online
View Journal | View Issue

One-pot synthesis of cuboid WO_3 crystal and its gas sensing properties

Cite this: *RSC Adv.*, 2014, **4**, 18365

Chong Wang,[a] Xin Li,[a] Biao Wang,[b] Jian Ma,[a] Yang Cao,[a] Yanfeng Sun*[a] and Geyu Lu*[a]

Received 16th January 2014
Accepted 31st March 2014

DOI: 10.1039/c4ra00445k

www.rsc.org/advances

In this work, a simple solvothermal method was used for the synthesis of cuboid WO_3 crystals without any surface active agent. The calcined WO_3 was characterized using field emission scanning electron microscopy (FESEM), X-ray powder diffraction (XRD) and transmission electron microscopy (TEM). The results indicate that the sample is composed of cuboid nanobulks. The gas sensing property of a sensor based on the cuboid WO_3 was also investigated. It is found that the sensor has a high response to low concentration NO_2 at low operation temperature, so the cuboid nanobulks might have a potential application in the fabrication of highly sensitive and low power consumption NO_2 gas sensors.

1. Introduction

With the increasing attention on atmospheric pollution, the detection of harmful gases at low concentrations becomes an important issue. So, a lot of effort has been devoted to the exploration of new material with enhanced gas sensing performance in recent years. The existing gas sensor materials include semiconducting metal oxides,[1,2] silicon,[3,4] organic[5,6] and fiber optic chemical materials.[7,8] Among them, semiconducting metal oxides have gained much more focus due to their superior properties. Up to now, a variety of semiconductor nanomaterials have been successfully synthesized, such as ZnO,[9,10] SnO_2,[11,12] CuO,[13,14] Fe_2O_3 (ref. 15 and 16) and In_2O_3.[17,18] As is well known, NO_2 is a highly harmful gas among the toxic gases, causing acid rain and photochemical smog, and further affecting people's health, even their lives. WO_3 is found to show a high response to NO_2 with high selectivity.[19,20] However, achieving a high response to ppb levels of NO_2 is still a challenge.

In order to improve the performance of the sensors based on WO_3, various structures with different morphologies have been investigated: nanoplates,[21] nanorods,[22] nanospheres,[23] nanoflowers[24] and other hierarchically complex architectures. At the same time, different physical and chemical synthetic methods have also been explored to obtain WO_3 crystals.[25–28] Among all these methods, the solvothermal method is considered a simple and practicable operation to synthesize high yield crystals with good monodispersity. Moreover, this low-cost synthesis is also a key point of researchers' pursuit all the time. Consequently, it is strongly desirable to develop a simple, effective, and economical approach for the synthesis of WO_3 with excellent NO_2 sensing performance.

Herein, we report a facile method for the preparation of WO_3 crystals by a simple process. Further, sensing performance based on the calcined WO_3 nanocrystal is also investigated here. It is found that the sensor showed a high response to ppb levels of NO_2 at 100 °C.

2. Experimental

2.1. Synthesis and characterization of WO_3 nanobulks

All the reagents (analytical-grade purity) were used without any further purification. In a typical synthesis, 10 mL glycerol and 25 mL distilled water were mixed together by stirring. One hour later, 0.66 g sodium tungstate was added to the solution to form a homogeneous solution. Then, 2.5 mL 12 M HCl was dropped to the sodium tungstate solution, and yellow precipitates formed. Five minutes later, the above solution was transferred into a Teflon-lined stainless steel autoclave, sealed tightly, and maintained at 180 °C for 12 h. After the autoclave was cooled to room temperature naturally, the precipitates were washed with deionized water and absolute ethanol several times using centrifuge, and then dried at 80 °C for 24 h. The precipitates were calcined at 500 °C for 2 h with a heating rate of 2 °C min^{-1}. The calcined products were then collected for further analysis.

X-ray power diffraction (XRD) analysis was conducted on a Rigaku D/max-2500 X-ray diffractometer with Cu Kα1 radiation ($\lambda = 1.54056$ Å) in the range of 20–60°. The morphology was examined by field-emission scanning electron microscopy (FESEM, JEOL JSM-7500F, operated at an acceleration voltage of 15 kV). Transmission electron microscopy (TEM)

[a]*State Key Laboratory on Integrated Optoelectronics, College of Electronic Science and Engineering, Jilin University, Changchun 130012, People's Republic of China. E-mail: syf@jlu.edu.cn; lugy@jlu.edu.cn; Fax: +86 431 85167808; Tel: +86 431 85167808*
[b]*State Key Laboratory of Luminescence and Application, Changchun Institute of Optics, Fine Mechanics and Physics, Chinese Academy of Sciences, Changchun 130033, China*

and selected-area electron diffraction (SAED) were obtained on a JEOL JEM-2100 microscope operated at 200 kV.

2.2. Fabrication and measurement of sensor

The calcined powders were mixed with deionized water to form a paste, which was then coated onto an alumina tube (4 mm in length, 1.2 mm in external diameter and 0.8 mm in internal diameter) using a small brush, slowly and lightly. The tube was installed with a pair of gold electrodes, and each electrode was connected with two Pt wires. After brushing, a thick film was formed. After drying at room temperature, the sensing device was then sintered at 300° for 2 h in air. Finally, a Ni–Cr alloy coil was inserted into the alumina tube as a heater in order to control the operating temperature of the sensor. A schematic structure of the as-fabricated sensor is shown in Fig. 1a.

The gas sensing property of the sensor was measured by a static process, and the schematic diagram is given in Fig. 2b. The resistance in the chamber (the volume is 50 L) filled with air is R_a, and then a certain amount of target gas is injected into this closed chamber. When the resistance reached R_g, the gas is discharged with the help of an air blower and fan. The data are collected by digital precision multimeter every second. $S = R_g/R_a$ is defined as the response of the sensor for oxidizing gas and R_a/R_g for reducing gas; here, R_a and R_g is the resistance of the sensor in the air and target gas.

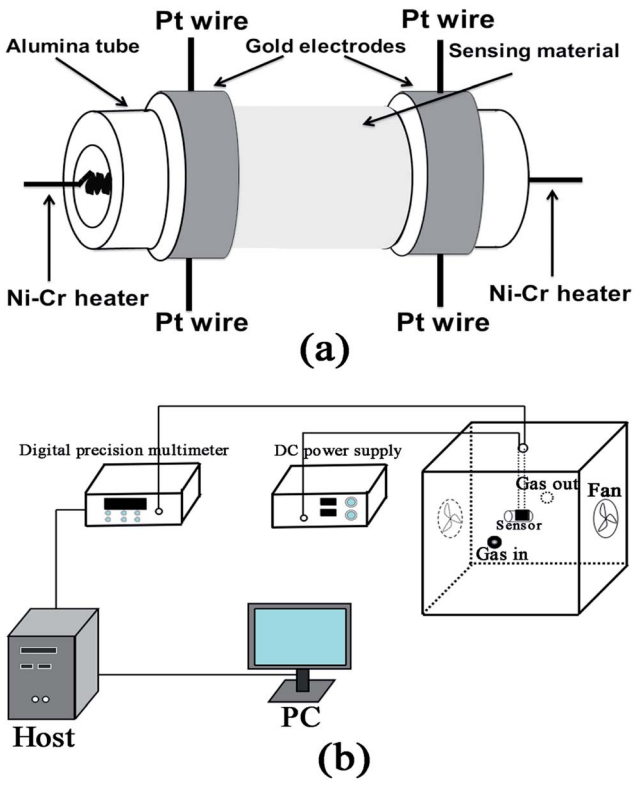

Fig. 1 (a) Schematic structure of the gas sensor. (b) The testing schematic diagram.

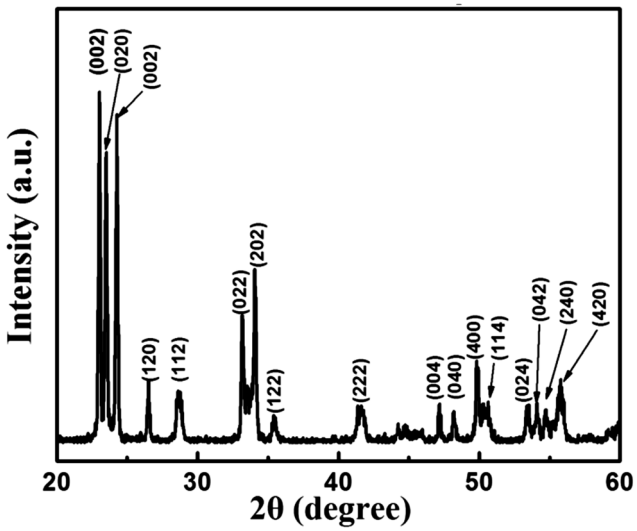

Fig. 2 X-ray diffraction patterns of the calcined product.

3. Results and discussion

3.1. Structural and morphological characteristics of the calcined WO_3

The X-ray diffraction (XRD) patterns of the calcined products are shown in Fig. 2. It can be seen from Fig. 2 that all of the diffraction peaks can be well indexed to the standard WO_3 (JCPDS file no. 83-950). No other diffraction peaks from any impurities are observed, indicating the high purity of the product. The XRD patterns (not shown here) of the sample without calcination are almost the same as the calcined products.

The morphology of the calcined product was investigated by field emission scanning electron microscopy (FESEM). The typical SEM images are shown in Fig. 3a and b. As can be seen from Fig. 3a and b, the products are mostly composed of cuboid

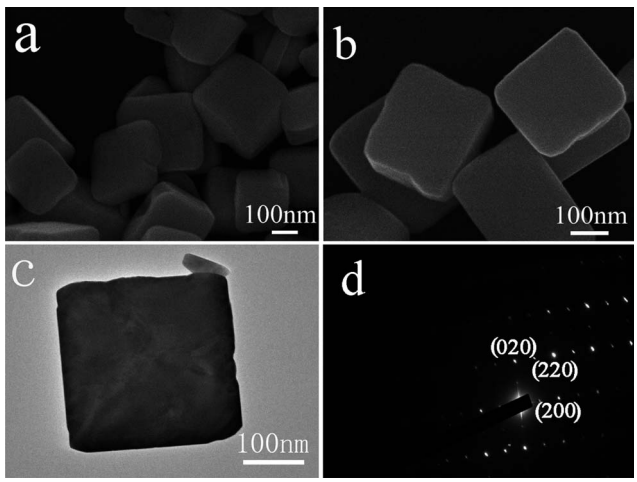

Fig. 3 (a and b) Typical SEM images of the calcined product. (c) TEM image of the WO_3 cubic nanobulks. (d) The corresponding SAED pattern.

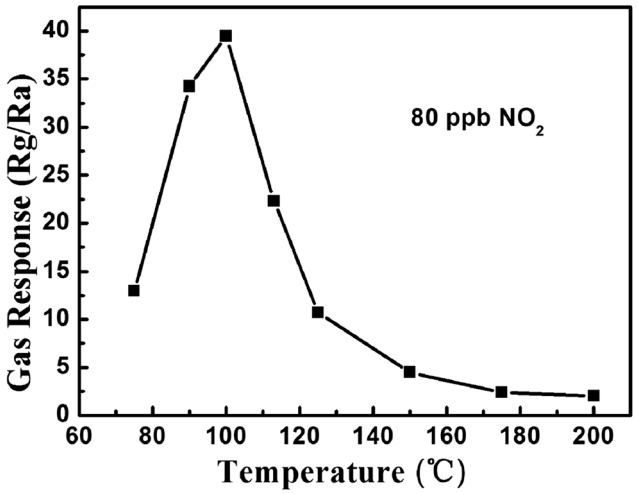

Fig. 4 Correlations between the gas response and response time to 80 ppb NO_2 and the operating temperature for the sensor using the as-obtained WO_3.

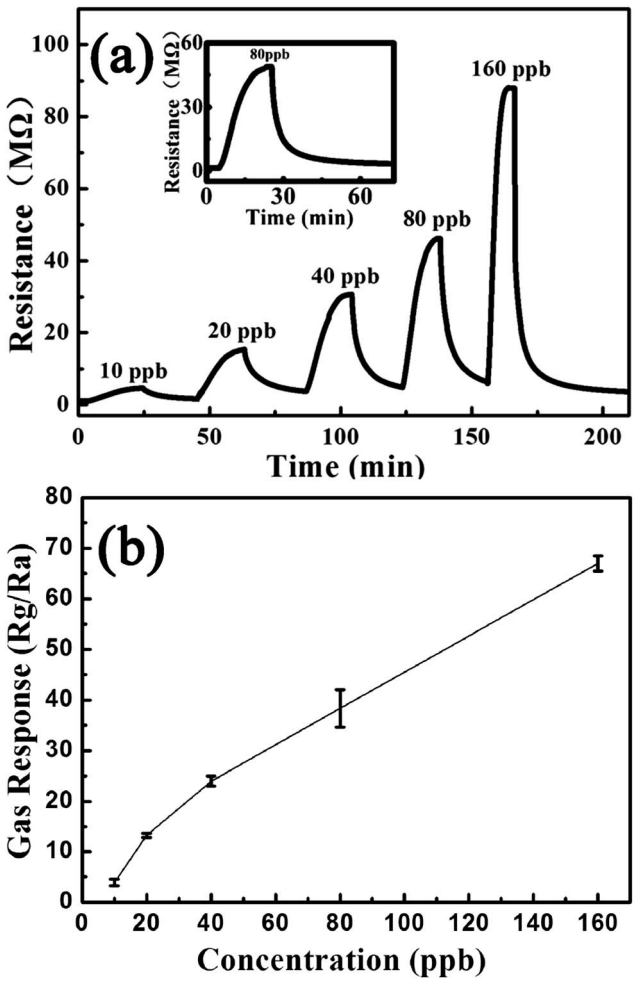

Fig. 5 (a) Response transients of the sensor to different NO_2 concentration at 100 °C. (b) Gas response of the sensor as a function of NO_2 concentrations. Error bars are the standard deviations.

three-dimensional nanobulks. The TEM image is shown in Fig. 3c; an individual typical cuboid three-dimensional nanobulk is also observed, which agrees with the SEM results. The selected area electron diffraction pattern (SAED) was also performed on the calcined products, as shown in Fig. 3d, which confirmed that the nanobulks are single crystalline monoclinic WO_3.

3.2. Gas sensing properties for NO_2

The sensing properties of a sensor based on the as-prepared WO_3 samples were investigated. In order to determine the optimum operating temperature, the response of the sensor to 80 ppb NO_2 was measured at different temperatures. As shown in Fig. 4, the response of the sensor increases from 75 °C to 100 °C. When the temperature further increases above 100 °C, the response begins to decrease gradually. This phenomenon could be explained as follows: at low temperatures (between 75 °C and 100 °C), the increase of the response can be attributed to the increase of the surface reaction ($NO_{2(g)} + e^- \rightarrow NO_2^-{}_{(ads)}$). Such adsorption can capture the electrons from WO_3, resulting in the increased electrical resistance. However, when the temperature is higher (between 100 °C and 200 °C), the chemi-adsorbed oxygen becomes larger and plays a significant role ($O_{(ads)}^{2-} + NO_2 \rightarrow NO_2^-{}_{(ads)} + e^-$), and this kind of reaction goes against the adsorption of NO_2. On the other hand, the rate of adsorption is lower compared to desorption at the higher temperature, which might be another reason for the decrease of the sensor's response.[35–37] Accordingly, at the temperature of the maximum response, the optimum balance between adsorption and desorption has been established for the NO_2 molecules. Therefore, the optimal working temperature of 100 °C is chosen to further examine the characteristics of the gas sensor.

The response transient curve of the sensor to stepwise increase of the NO_2 concentration from 0 to 160 ppb at optimum operating temperature is shown in Fig. 5a. The inset is the resistance transient in the presence of only 80 ppb

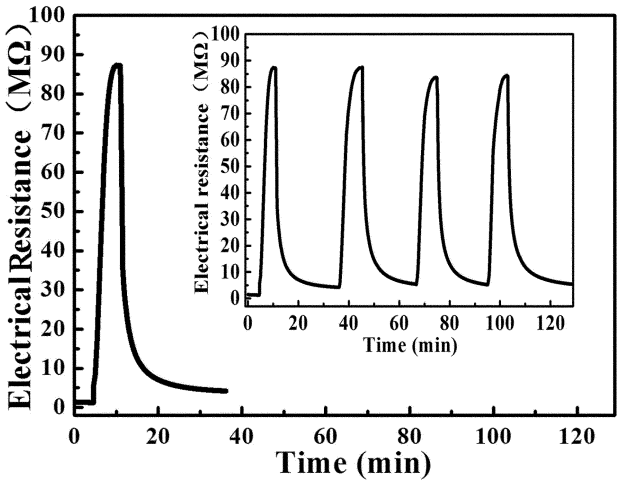

Fig. 6 Response transients of the sensor to 160 ppb NO_2 at 100 °C, the inset displaying four periods of response curve.

Table 1 Gas responses to NO_2 in the present study and those reported in the literature

Material	Preparation	NO_2 concentration	Operating temperature	Response	Reference
WO_3	Hydrothermal	40 ppb	100°	23	Present study
WO_3	Acidification	50 ppb	200°	13	29
WO_3	Thermal evaporation	100 ppb	100°	18.2	30
WO_3	Template method	1 ppm	230°	9	31
WO_3	Hydrothermal	1 ppm	200°	13.4	32

of NO_2. It is obvious that the resistance increases when exposed to gradually increased concentrations of NO_2. In other words, the response increases with increasing concentration. The relationship between the response of the sensor and the concentration of NO_2 is shown in Fig. 5b; the error bars are also displayed. The error bars represent the standard deviation at a fixed concentration, and they are small in all cases, which means a low experimental variability. It is worth noting that this sensor responds to low concentrations of NO_2, and even the 10 ppb NO_2 can also be detected. The response transients of the sensor to 160 ppb NO_2 was measured at 100 °C (Fig. 6). The four reversible cycles of the response curve indicate a stable and repeatable characteristic, as shown in the inset of Fig. 6. A comparison between the sensing performances of the sensor fabricated in our work and in literature reports is summarized in Table 1. From the comparison, it can be seen that the sensor based on cuboid WO_3 crystals has a correspondingly high response and low operating temperature. The high response of this cuboid nanobulk material may be attributed to the following reasons. On one hand, the product has a good crystalline character. The high crystallization will result in low bulk defects, thus lowering the conductivity of the sensing body. Due to this reason, only a small amount of NO_2 adsorption will cause the resistance to change greatly. The conductivity of the sensor with the variation of operating temperature is also shown in Fig. 7; it can be clearly observed that the conductivities increase rapidly between 50 °C and 75 °C, and then increase slowly between 75 °C and 200 °C. On the other hand, the cuboid structure has trim edges, which will form grain boundaries in the sensing body. According to Li *et al.*[33] and Hyodo *et al.*,[34] grain boundaries or grain junctions are considered as the active sites, and they act positively on the sensor response. Therefore, the sensor is expected to have a high response to NO_2.

It is well known that selectivity is another important parameter of a sensor in view of its practical application; therefore, at the optimum operating temperature, the response of the cuboid nanobulk-based sensor to various kinds of gases, such as Cl_2, CO, H_2S, NH_3, acetone and ethanol, was investigated. The results are shown in Fig. 8 with error bars. It can be seen that the sensor has a high response to NO_2 compared to the other gases. Such result demonstrates that the sensor using the WO_3 nanostructure synthesized here exhibits an excellent selectivity to NO_2 against the other tested gases at the working temperature of 100 °C.

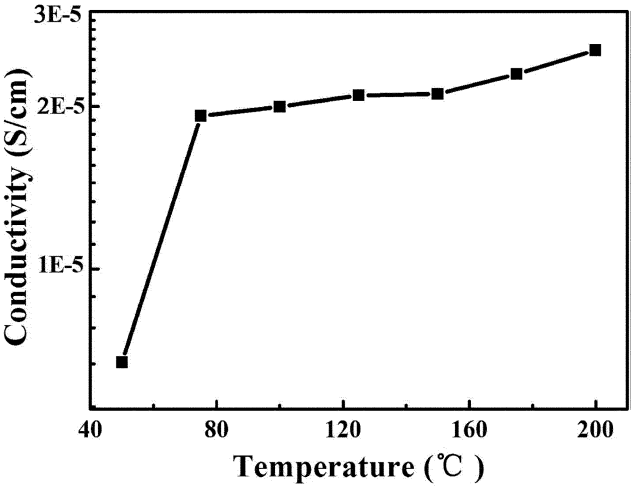

Fig. 7 Conductivity of the sensor as a function of operating temperature.

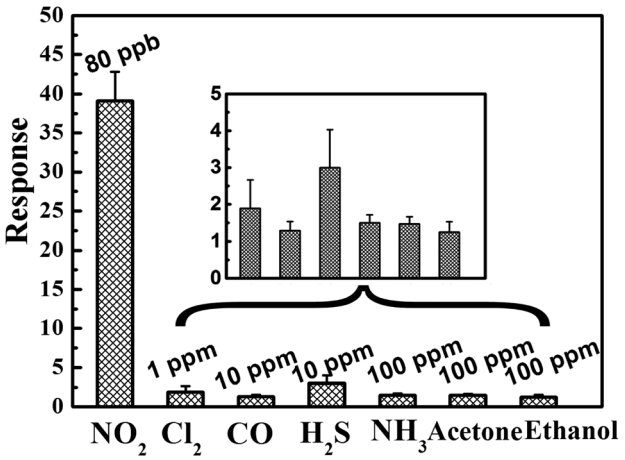

Fig. 8 Comparison of responses of the sensor based on WO_3 to various gases at 100 °C. Error bars represent the variability obtained in measurements.

4. Conclusion

In summary, cuboid WO_3 crystal has been successfully synthesized through a simple one-step solution route combined with a subsequent calcining process. Field emission scanning electron microscopy and transmission electron microscopy results demonstrate that the products are composed of nanobulks and

that they are single crystal. In addition, the gas sensing properties of the calcined WO_3-based sensor toward NO_2 were investigated. The sensor based on the cuboid WO_3 nanobulks exhibits excellent NO_2 sensing properties at 100 °C. In particular, the response to 40 ppb reaches 23 at 100 °C. These results indicate that our sensor might have potential application in fabricating highly sensitive and low power consumption NO_2 gas sensor devices.

Acknowledgements

This work is supported by Application and Basic Research of Jilin Province (20130102010JC), the National Nature Science Foundation of China (no. 61304242, 61327804, 61134010 and 61374218), Program for Chang Jiang Scholars and Innovative Research Team in University (no. IRT13018) and "863" High Technology Project (2013AA030902).

References

1 N. Yamazoe, G. Sakai and K. Shimanoe, *Catal. Surv. Asia*, 2003, **7**, 63–75.
2 N. Yamazoe, *Sens. Actuators, B*, 1991, **5**, 7–19.
3 S. E. Lewis, J. R. DeBoer, J. L. Gole and P. J. Hesketh, *Sens. Actuators, B*, 2005, **110**, 54–65.
4 L. Boarino, C. Baratto, F. Geobaldo, G. Amato, E. Comini, A. M. Rossi, G. Faglia, G. Lérondel and G. Sberveglieri, *Mater. Sci. Eng., B*, 2000, **69-70**, 210–214.
5 O. S. Wolfbeis, *Anal. Chem.*, 2006, **78**, 3859–3874.
6 R. C. Jorgenson and S. S. Yee, *Sens. Actuators, B*, 1993, **12**, 213–220.
7 L. Torsi, A. Dodabalapur, L. Sabbatini and P. G. Zambonin, *Sens. Actuators, B*, 2000, **67**, 312–316.
8 K. H. An, S. Y. Jeong, H. R. Hwang and Y. H. Lee, *Adv. Mater.*, 2004, **16**, 1005–1009.
9 B. B. Rao, *Mater. Chem. Phys.*, 2000, **64**, 62–65.
10 S. Roy and S. Basu, *Bull. Mater. Sci.*, 2002, **25**, 513–515.
11 J. Watson, *Sens. Actuators, B*, 1984, **5**, 29–42.
12 A. Maiti, J. A. Rodriguez, M. Law, P. Kung, J. R. McKinney and P. D. Yang, *Nano Lett.*, 2003, **3**, 1025–1028.
13 J. T. Zhang, J. F. Liu, Q. Peng, X. Wang and Y. D. Li, *Chem. Mater.*, 2006, **18**, 867–871.
14 Y. S. Kim, I. S. Hwang, S. J. Kim, C. Y. Lee and J. H. Lee, *Sens. Actuators, B*, 2008, **135**, 298–303.
15 J. Chen, L. Xu, W. Li, X. Gou, J. Chen, L. Xu, W. Li and X. Gou, *Adv. Mater.*, 2005, **17**, 582–586.
16 P. Sun, Y. W. Liu, X. W. Li, Y. F. Sun, X. S. Liang, F. M. Liu and G. Y. Lu, *RSC Adv.*, 2012, **2**, 9824–9829.
17 T. Waitz, T. Wagner, T. Sauerwald, C. D. Kohl and M. Tiemann, *Adv. Funct. Mater.*, 2009, **19**, 653–661.
18 X. M. Xu, X. Li, W. B. Wang, B. Wang, P. Sun, Y. F. Sun and G. Y. Lu, *RSC Adv.*, 2014, **4**, 4831–4835.
19 X. L. Li, T. J. Lou, X. M. Sun and Y. D. Li, *Inorg. Chem.*, 2004, **43**, 5442–5449.
20 B. B. Cao, J. J. Chen, X. J. Tang and W. L. Zhou, *J. Mater. Chem.*, 2009, **19**, 2323–2327.
21 J. M. Ma, J. Zhang, S. R. Wang, T. H. Wang, J. B. Lian, X. C. Duan and W. J. Zheng, *J. Phys. Chem. C*, 2011, **115**, 18157–18163.
22 J. M. Wang, E. Khoo, P. S. Lee and J. Ma, *J. Phys. Chem. C*, 2008, **112**, 14306–14312.
23 Q. J. Sun, J. M. Luo, Z. F. Xie, J. D. Wang and X. T. Su, *Mater. Lett.*, 2008, **62**, 2992–2994.
24 J. R. Huang, X. J. Xu, C. P. Gu, G. J. Fu, W. Z. Wang and J. H. Liu, *Mater. Res. Bull.*, 2012, **47**, 3224–3232.
25 J. Zhou, Y. Ding, S. Z. Deng, L. G. Ning, S. Xu and Z. L. Wang, *Adv. Mater.*, 2005, **17**, 2110–2114.
26 Y. Djaoued and S. Balaji, *J. Sol-Gel Sci. Technol.*, 2013, **65**, 374–383.
27 J. Zhang, J. P. Tu, X. H. Xia, X. L. Wang and C. D. Gu, *J. Mater. Chem.*, 2011, **21**, 5492–5498.
28 A. Phuruangrat, D. J. Ham, S. J. Hong, S. Thongtem and J. S. Lee, *J. Mater. Chem.*, 2010, **20**, 1683–1690.
29 T. Kida, A. Nishiyama, M. Yuasa, K. Shimanoe and N. Yamazoe, *Sens. Actuators, B*, 2009, **135**, 568–574.
30 A. Ponzoni, E. Comini, M. Ferroni and G. Sberveglieri, *Thin Solid Films*, 2005, **490**, 81–85.
31 E. Rossinyol, A. Prim, E. Pellicer, J. Arbiol, F. H. Ramírez, F. Peiró, A. Cornet, J. R. Morante, L. A. Solovyov, B. Tian, T. Bo and D. Y. Zhao, *Adv. Funct. Mater.*, 2007, **17**, 1801–1806.
32 Y. X. Qin, M. Hu and J. Zhang, *Sens. Actuators, B*, 2010, **150**, 339–345.
33 E. Li, Z. X. Cheng, J. Q. Xu, Q. Y. Pan, W. J. Yu and Y. L. Chu, *Cryst. Growth Des.*, 2009, **9**, 2146–2151.
34 T. Hyodo, N. Nishida, Y. Shimizu and M. Egashira, *Sens. Actuators, B*, 2002, **83**, 209–215.
35 G. Lu, N. Miura and N. Yamazoe, *Ionics*, 1998, **4**, 16–24.
36 X. Q. An, J. C. Yu, Y. Wang, Y. M. Hu, X. L. Yu and G. J. Zhang, *J. Mater. Chem.*, 2012, **22**, 8525–8531.
37 A. P. Lee and B. J. Reedy, *Sens. Actuators, B*, 1999, **60**, 35–42.